All-Optical MIMO Demultiplexing Using Silicon-Photonic Dual-Polarization Optical Unitary Processor

Ryota Tanomura, *Member, IEEE*, Rui Tang, Go Soma, Shota Ishimura, Takuo Tanemura, *Member, IEEE*, and Yoshiaki Nakano, *Fellow, IEEE*

(Top-Scored Paper)

***Abstract*—Dual-polarization (DP) arbitrary optical unitary processor (OUP) is a critical device to realize an energy-efficient multi-input-multi-output (MIMO) process of mode-division multiplexed (MDM) systems in the optical domain. In this article , a 6-port OUP with polarization-splitter-rotators is realized on a compact silicon photonic chip based on the multi-plane light conversion (MPLC) concept. All-optical MIMO demultiplexing of 300-Gbps 3-mode DP quadrature phase-shift-keying (QPSK) signal is demonstrated at 1540, 1550, and 1560-nm wavelengths with an energy consumption of around 1.5 pJ/bit. Since all-optical MIMO is transparent to the signal format, the energy cost (J/bit) would decrease inversely as we increase the baudrate, making it an attractive approach in reducing the power consumption of the future ultra-high-capacity MDM systems.**

***Index Terms*—Mode demultiplexing, mode-division multiplexing (MDM), programmable photonics, silicon photonics.**

I. Introduction

MODE-DIVISION multiplexing (MDM) is the key technology that enables Peta-bit/s-class ultra-high-capacity optical communication systems [1], [2]. In MDM systems using multimode fibers (MMFs) or multi-core fibers (MCFs), modal crosstalk occurs due to the inevitable inter-modal coupling during the transmission. To compensate for this crosstalk, multi-input-multi-output (MIMO) demultiplexing process is required at the receiver to retrieve the original signals [3]. While this is typically performed through the electronic digital signal processing (DSP) after coherent detection [1], [2], [4], [5], [6], [7], [8], its complexity and power consumption scale super-linearly as the number of modes increases [9].

To cope with this problem, all-optical MIMO demultiplexer has been considered [10], [11], [12]. As shown in Fig. 1, an all-optical MIMO circuit at the receiver can unscramble mixed multimode optical signals with nominal power consumption, which is transparent to the signal baudrate and the modulation format. In particular, fully integrated all-optical MIMO devices are attractive in terms of footprint and power consumption. To date, several types of all-optical MIMO demultiplexers have been demonstrated on compact silicon photonic platforms, based on arrays of Mach-Zehnder interferometers [11] and tunable splitters [12]. These experimental demonstrations were, however, limited to either a single-polarization operation without using an actual MMF link [11] or with a single-output-channel device that could only demultiplex multiple channels sequentially [12].

To this end, we have recently developed dual-polarization (DP) arbitrary optical unitary processor (OUP) to demonstrate simultaneous all-optical MIMO demultiplexing of DP 3-mode-multiplexed signals [13]. The DP-OUP consists of polarization-splitter-rotators (PSRs) attached at the three input ports, followed by a 6-port arbitrary OUP circuit to unscramble both the spatial and polarization modes in a reconfigurable manner. Using the fabricated device, we have experimentally demonstrated demultiplexing of 3-mode 25-Gbaud DP quadrature-phase-shift-keying (QPSK) signals (300 Gbps in total). In this article, we provide detailed design procedures, numerical analyses, and characterization of the PSR section, as well as additional experimental results on the wavelength dependence of all-optical MIMO performance.

II. Structure and Principle of Dual-Polarization Optical Unitary Processor

The schematic of the 3-mode DP-OUP is shown in Fig. 2. Three DP signals, which are connected from a fan-out device (e.g., photonic lantern) as shown in Fig. 1, are polarization-demultiplexed by an integrated PSR attached at each port. The output ports of the PSRs are then guided to a 6-port OUP circuit based on the multi-plane light conversion (MPLC) scheme [14], [15], [16], [17], where appropriate linear transformation can be

Manuscript received 29 November 2022; revised 20 March 2023; accepted 29 April 2023. Date of publication 17 May 2023; date of current version 27 June 2023. This work was supported in part by MbSC2030 and in part by the Japan Society for the Promotion of Science (JSPS) under Grants JP20J221861 and JP21K1816. *(Corresponding authors: Ryota Tanomura; Takuo Tanemura.)*

Ryota Tanomura, Rui Tang, Go Soma, Takuo Tanemura, and Yoshiaki Nakano are with the Department of Electrical Engineering and Information Systems, School of Engineering, The University of Tokyo, Tokyo 113-8656, Japan (e-mail: ryota_tanomura@hotaka.t.u-tokyo.ac.jp; ruitang@mosfet.t.u-tokyo.ac.jp; soma@hotaka.t.u-tokyo.ac.jp; tanemura@ee.t.u-tokyo.ac.jp; nakano@ee.t.u-tokyo.ac.jp).

Shota Ishimura is with the KDDI Research, Inc., Fujimino 356-8502, Japan (e-mail: sh-ishimura@kddi-research.jp).

Color versions of one or more figures in this article are available at https://doi.org/10.1109/JLT.2023.3276003.

Digital Object Identifier 10.1109/JLT.2023.3276003

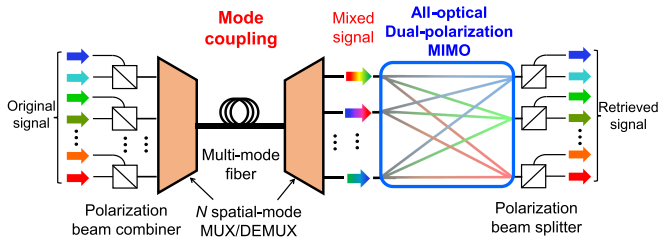

Fig. 1. Polarization-and mode-multiplexed transmission system using an all-optical DP MIMO demultiplexer. Note that different colors in the arrows are used for the ease of understanding and all channels are at the same wavelength.

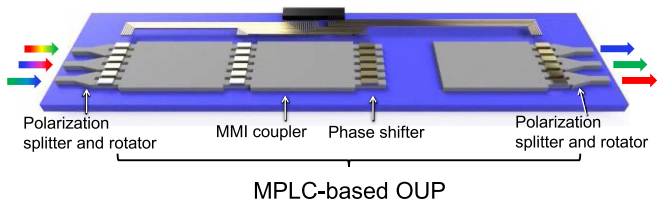

Fig. 2. Schematic of the all-optical DP-OUP chip demonstrated in this work. It consists of a PSR array section and an OUP section. Each PSR is realized by the adiabatic-polarization rotator and a mode-independent splitter. The OUP section consists of cascaded phase-shifter arrays and MMI couplers based on the MPLC concept.

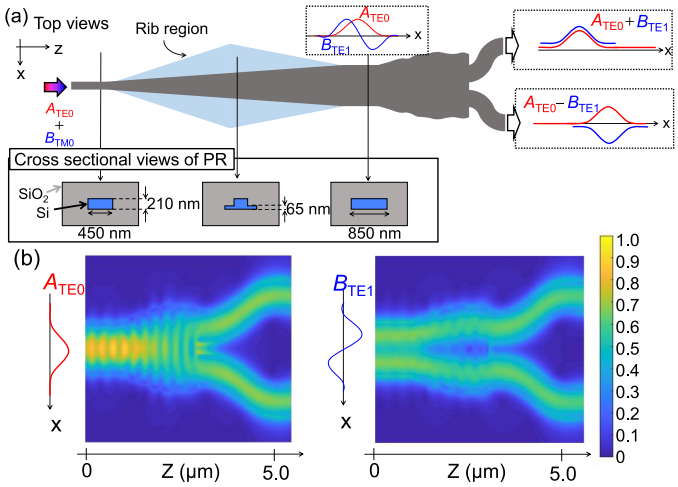

Fig. 3. (a) Schematic of the PSR based on the adiabatic mode converter and a mode-independent Y-splitter. (b) Simulated light propagation for the TE_0 and TE_1 input modes through the Y-splitter, which is designed using the PSO algorithm (see Appendix A for details).

applied to compensate for the effects of coupling among the spatial/polarization modes.

Fig. 3 shows the schematic of the integrated PSRs, which are similar to those used in our previous work [18]. It consists of an adiabatic mode converter based on the tapered rib waveguide [19], [20], [21], followed by a mode-independent Y-splitter. In the adiabatic mode-converting section, the width of the rib waveguide is tapered gradually as shown in Fig. 3(a), so that the 0-th transverse-magnetic (TM_0) mode is converted into the 1-st transverse-electric (TE_1) mode without loss.

The mode-independent Y-splitter is designed based on the particle swarm optimization (PSO) algorithm [22]. The details of the design procedures are explained in Appendix A. Fig. 3(b) shows the light propagation through the designed Y-splitter, simulated by the three-dimensional finite-difference time-domain method (3D-FDTD). As a result, the input DP signal with the complex amplitudes of a_{TE_0} and a_{TM_0} is split to two output ports with the amplitudes of $1/\sqrt{2}(a_{TE_0}+ a_{TM_0})$ and $1/\sqrt{2}\,(a_{TE_0}- a_{TM_0})$. We should note that unlike a typical PSR [19], [20], [21], it is not necessary to split TE_0 and TM_0 in our device since any linear coupling can be removed anyway at the OUP section.

The $N \times N$ OUP is based on the concept of MPLC, where N-mode interferometers and phase shifter arrays are cascaded in series [16], [23], [24], [25], [26], [27], [28]. Here, we use a multimode interference (MMI) coupler as the N-mode interferometers [29], [30]. The transfer matrix $\mathbf{U}$ of an MPLC-based OUP is written as

$$\mathbf{U} = \mathbf{\Phi}_L \cdot \mathbf{T} \cdot \mathbf{\Phi}_{L-1} \cdots \mathbf{\Phi}_0, \tag{1}$$

where L is the number of the cascaded stages, and $\mathbf{T}$ and $\mathbf{\Phi}_i$ ($i = 0, 1, \cdots, L$) are the transfer matrices of a MMI coupler and a phase shifter array, respectively. Each $\mathbf{\Phi}_i$ includes N phase shifters so that $N(L + 1)$ phase shifters in total are employed in this work. We should note that in principle, only $N - 1$ phase shifters are required except for the first stage ($i = 0$) [16]. Here, we integrate N phase shifters in all stages for convenience, so that the optical loss is balanced among different optical paths within the chip. The phase shifter arrays function as tunable phase-manipulating layers, while the MMI couplers provide fixed unitary transformations. As a result, according to the principle of MPLC, arbitrary unitary operation can be implemented when $L \geq N$ [14]. In this work, we set $L = 8$ and $N = 6$.

III. Device Characterization

A. 3-Port DP-OUP Fabricated on Si

Fig. 4 shows the photograph and the scanning-electron microscope (SEM) images of the 3-port DP-OUP fabricated on a silicon-on-insulator (SOI) platform with a 210-nm-thick silicon and 3-μm buried oxide (BOX) layers. The entire circuit fits within a footprint of 2.5 mm $\times$ 9.0 mm. The device consists of PSR arrays, 9 stages of thermo-optic (TO) phase shifter arrays with 200-μm-long TiN heaters, and 8 stages of 6 $\times$ 6 MMI couplers. The width and the length of an MMI coupler are set to 15 μm and 268 μm, respectively. The total number of phase shifters is 54. While PSRs are not necessary at the output, they are included in this work to reduce the number of ports that need to the coupled to the output fiber array.

From preliminary measurements, we derive the coupling loss between the fiber array and the chip to be 3.5 dB/facet, the insertion loss of the 6 $\times$ 6 MMI coupler to be 1.5 dB, and the propagation loss of the Si waveguide to be 2.7 dB/cm (TE) and 3.2 dB/cm (TM). The V_π of the phase shifter is around 3.1 V.

B. Characterization of Symmetric PSR

First, passive properties of a single PSR were characterized. Fig. 5(a) shows the experimental setup. A continuous-wave light

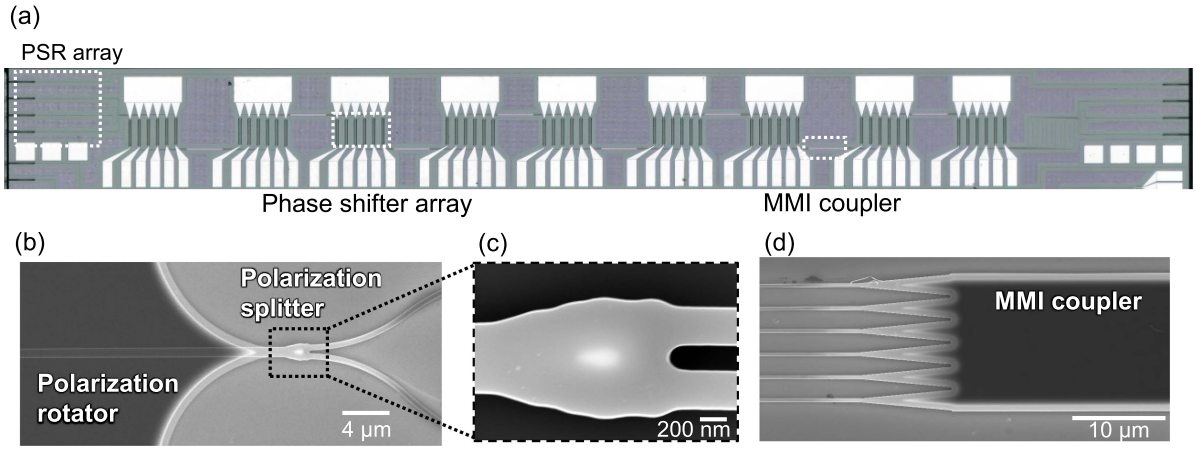

Fig. 4. (a) Microscope image. (b)–(d) The SEM images of (b) the entire PSR section, (c) enlarged Y-splitter, and (d) 6-port MMI coupler.

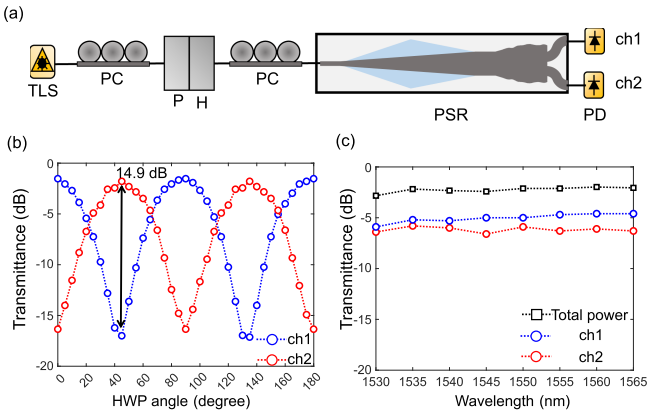

Fig. 5. Experimental setup for passive PSR characterization. TLS: tunable laser source, PC: polarization controller, P: polarizer, H: half-wave plate (HWP), PD: photodetector. (b) Measured transmittance of PSR as a function of the HWP angle at 1550-nm wavelength and (c) its wavelength dependence when the HWP angle is set to 20 deg for each wavelength.

from a tunable laser source (TLS) was launched to the device after its polarization state was controlled by a polarizer, a half-wave plate (HWP), and two fiber-based polarization controllers (PCs). The first PC was used to align the input polarization to the polarizer, while the second PC was adjusted to maximize the output power at channel 1. This corresponds to the case where the input light is split equally to TE_0 and TM_0 modes and interfere constructively after transmitting through the mode-converting section and the Y-splitter. By rotating the HWP, the input polarization state was rotated to the orthogonal state along a great circle on the Poincaré sphere [31].

Fig. 5(b) shows the transmittance of the PSR as a function of the HWP angle at 1550-nm wavelength. We can confirm that two orthogonal polarization states are split to the two output channels of the PSR with the polarization extinction ratio (PER) of 14.9 dB. Fig. 5(c) shows the transmittance as a function of wavelength when the HWP is set to 20 deg for each wavelength, corresponding to the case where the input light is split nearly equally to the two output ports. The deviation of transmittance in the *C* band is kept within 0.5 dB.

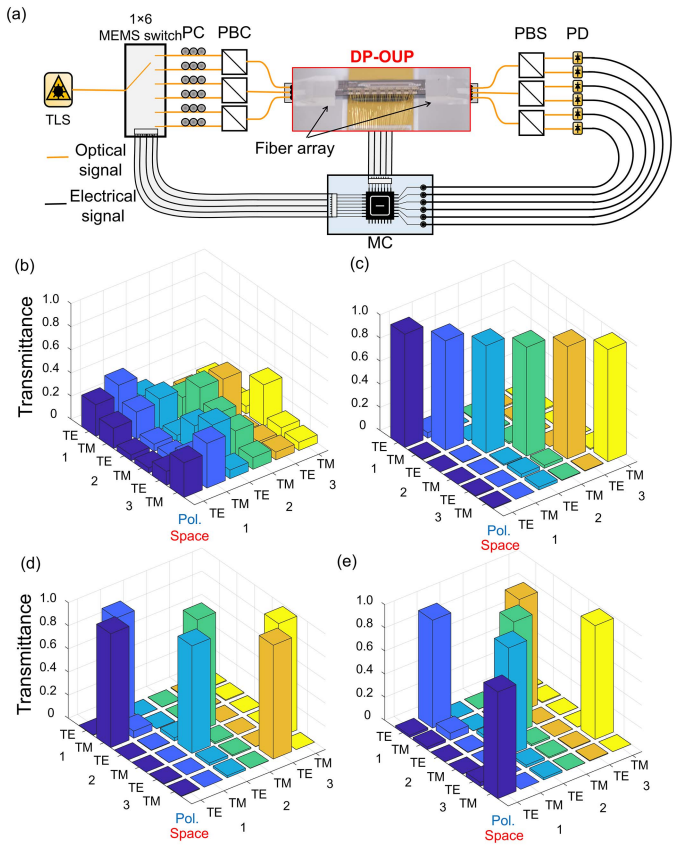

Fig. 6. (a) Experimental setup for measuring the DP-OUP performance. By sequentially changing the input port, the transmittance matrix of DP-OUP is measured and used as a feedback signal to optimize the TO phase shifters through the simulated annealing algorithm. TLS: tunable laser source, PC: polarization controller, PBC/PBS: polarization beam combiner/splitter, PD: photodetector, MC: microcontroller. (b)–(e) Measured transmittances from 6 input modes (3 spatial × 2 polarization) to 6 output modes (b) before optimization and (c)–(e) after optimization. In all cases, the crosstalk is suppressed to be less than −11 dB.

C. *Demonstration of 6-Mode DP-OUP*

We then measured the performance of the DP-OUP. The experimental setup is shown in Fig. 6(a). To test the DP operation, polarization beam combiners and splitters (PBCs and

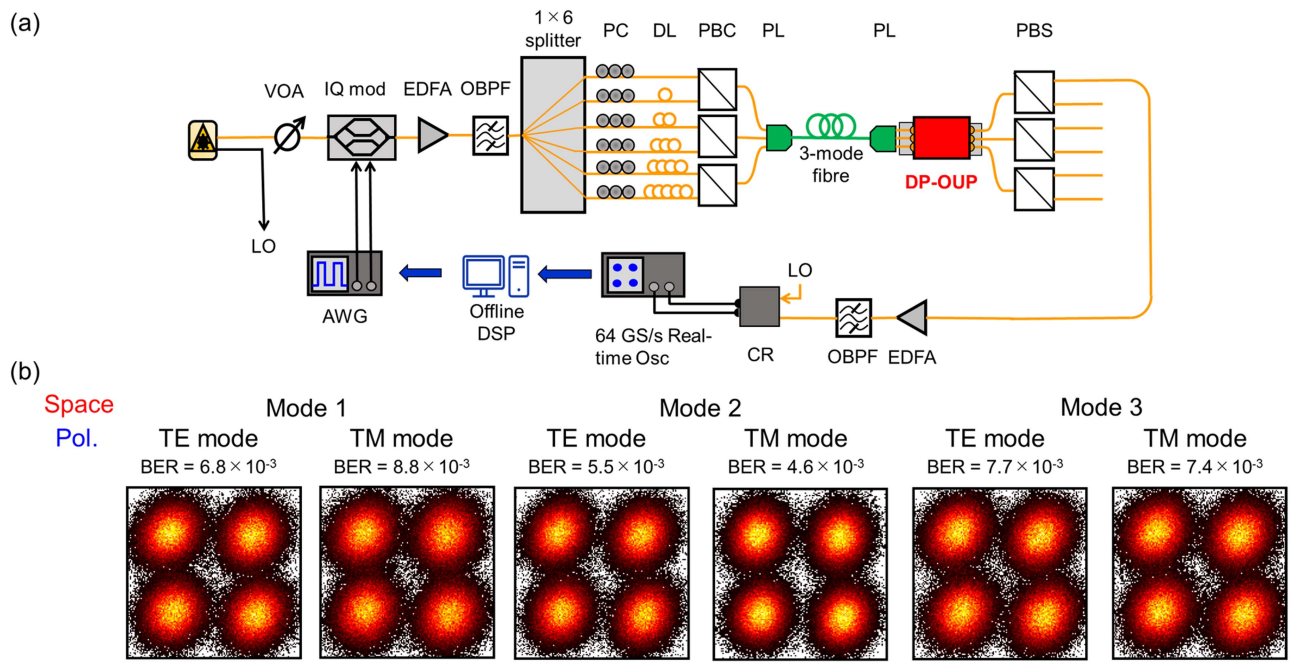

Fig. 7. (a) Experimental setup for all-optical MIMO demonstration with DP-QPSK signal. We generate the 25 Gbaud QPSK signal, and its signal is divided into 6 channels. After making each channel uncorrelated, polarization multiplexing using a polarization combiner and mode multiplexing using a photonic lantern are applied, and then the channels are combined into an MMF. Sending through the MMF, the modes of propagated light are again separated using a photonic lantern, and MIMO demultiplexing is performed using DP-OUP. VOA: variable optical attenuator, EDFA: erbium-doped fiber amplifier, OBPF: optical bandpass filter, PC: polarization controller, DL: delay line, PBC/PBS: polarization beam combiner/splitter, PL: photonic lantern, CR: coherent receiver, DSP: digital-signal processing, AWG: an arbitrary wave generator, LO: local oscillator. (b) Constellations of retrieved 50-Gbps QPSK signals after optical MIMO process and offline DSP.

PBSs) were inserted at the input and output ports. Similar to our previous work [27], the transmittances from all input ports to all output ports of DP-OUP were measured sequentially by controlling the 1×6 micro-mechanical-electrical-system (MEMS) switch. The phase shifters were then optimized through the simulated annealing algorithm to minimize the error between the target matrix and the measured matrix.

Fig. 6(b)–(d) show the measured transmission matrices at 1550 nm wavelength. While severe crosstalk is observed before optimization [see Fig. 6(b)], arbitrary mode-sorting matrices are obtained in a reconfigurable manner after adjusting the phase shifters [see Fig. 6(c) and (d)]. In all cases, the crosstalk is suppressed to be less than -11 dB.

IV. All-optical MIMO Experiments Using DP-OUP

Finally, all-optical MIMO experiments were carried out using the setup shown in Fig. 7(a). A $LiNbO_3$ in-phase and quadrature (IQ) modulator was driven by a two-channel arbitrary waveform generator (AWG) to generate a 25-Gbaud quadrature phase-shift-keying (QPSK) signal. The signal was split into six branches, decorrelated by fiber delay lines (DLs) to mimic an actual MDM system with six independent IQ signals, and combined by three PBCs and a photonic lantern (PL). For the proof-of-concept demonstration, we employed a 1-m-long 3-mode MMF in this work. While the length of MMF was short, MUX/DEMUX using PLs provided sufficient modal coupling to mimic an actual MDM system with crosstalk. We should note that the mode-dependent loss of the entire link was small enough and the inter-modal coupling could be assumed to be a unitary process. At the output of MMF, the signal was split by another PL and input to the DP-OUP. The optimization of DP-OUP was achieved following the same procedure as described in the previous section. In this experiment, the environmental drift was sufficiently slow so that active tracking was not necessary during the measurement. To be deployed in actual transmission systems with larger drift, we could implement the real-time mode/polarization tracking function by using similar techniques as demonstrated previously [11], [32], [33].

The output signals from the chip were separated by PBSs to receive each spatial/polarization mode by a coherent receiver (CR). Through offline DSP, the measured signals were down-sampled and then equalized by half-symbol-spaced adaptive finite-impulse-response (FIR) filters. We employed the decision-driven least-mean-square (DD-LMS) algorithm, which was the same procedure as used in [34]. We should stress that the MIMO processing for undoing the strong mixing among the spatial and polarization modes was performed in the optical domain and not by the DSP. As a result, we could substantially reduce the DSP cost, which would otherwise increase super-linearly with the number of spatial/polarization modes [9].

Fig. 7(b) shows the constellation diagrams of 50-Gbps QPSK signals for all three spatial modes and both polarizations. In all cases, we obtain BERs below the 20% soft-decision forward-error-correction (SD-FEC) threshold. The residual penalty is partially attributed to the imperfect mode demultiplexing inside the OUP section, as shown in Fig. 6. We thus expect it could be reduced by improving the PRS design and by using a more efficient optimization algorithm instead of the simulated annealing.

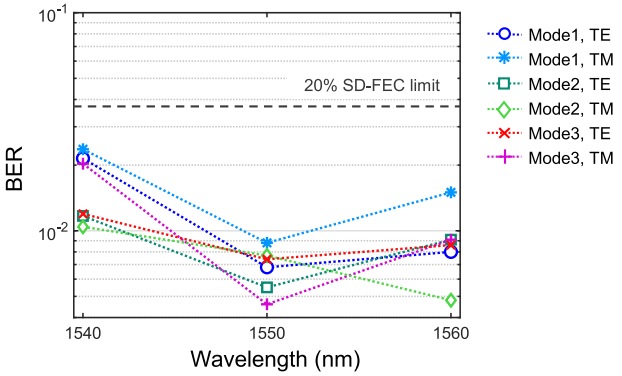

Fig. 8. Wavelength dependency of all-optical MIMO process. In all cases, the BER is less than the 20% SD-FEC limit.

Design mode-independent Y-splitter

randomly generate the initial set of $\mathbf{W}=\{\mathbf{w}_s\}$, where each element $\mathbf{w}_s$ is $\{w_1, w_2 \cdots, w_{13}\}$ $(n=1, \cdots, S)$
for $g = 1, 2, \cdots, G$ **do**
  for $s = 1, 2, \cdots, S$ **do**
    define the structure based on $\mathbf{w}_s$
    calculates the propagation with TE_0 and TE_1-mode light
    gets the transmittance at each output port.
    calculate the cost function f_s
  end for
  update $\mathbf{w}_s \in \mathbf{W}$ based on each value f_s and the PSO algorithm
end for
save the best $\mathbf{w}$ as the optimized parameters

Fig. 9. Procedure of optimizing mode-independent Y-splitter.

Fig. 8 compares the obtained BERs of 25-Gbaud DP-QPSK signal after all-optical MIMO process at different wavelengths. In all cases, BERs below the 20% SD-FEC limit are obtained. This broadband property of the device owes to the symmetrical and wavelength-independent MMI couplers as well as inherent robustness of the MPLC-based OUP [35].

The total power consumed at 54 phase shifters is derived to be around 450 mW. This corresponds to an energy cost of around 1.5 pJ/bit for the 300-Gbps signal demonstrated in this work. As a unique advantage of the all-optical MIMO, the power consumption is independent of the bitrate. This implies that the energy cost (J/bit) would decrease inversely as we increase the bitrate of the signal.

V. Conclusion

We have developed a silicon-photonic DP 3-mode OUP circuit and experimentally demonstrated all-optical MIMO demultiplexing of space/polarization-multiplexed coherent signals. The device consisted of adiabatic PSR arrays and an MPLC-based 6-port OUP circuit, integrated on a compact silicon chip with a footprint of 2.5 mm $\times$ 9.0 mm. A 300-Gbps DP 3-mode-multiplexed QPSK signal was demultiplexed successfully with the BER below the 20% SD-FEC threshold for all channels. Thanks to the inherent robustness of the MPLC-based OUP and the broadband symmetric MMI couplers used in the circuit, wideband operation from 1540-nm to 1560-nm wavelength range was confirmed. The energy consumption was derived to be around 1.5 pJ/bit, which can be reduced further as we increase the baudrate. The demonstrated device would thus pave the way for realizing the future cost- and power-efficient MDM transmission systems

Appendix

A. Design of Mode-Independent Y-Splitter

The mode-independent Y-splitter is designed based on the PSO scheme [22]. We first define the design area of the Y-splitter to be 2 μm $\times$ 2.6 μm. This region is then divided into 13 sections with an equal length of 200 nm. We define $\mathbf{w} = \{w_1, w_2, \cdots, w_{13}\}$ to describe the width at the center of each section. The actual geometry of the Y-splitter is represented by the spline

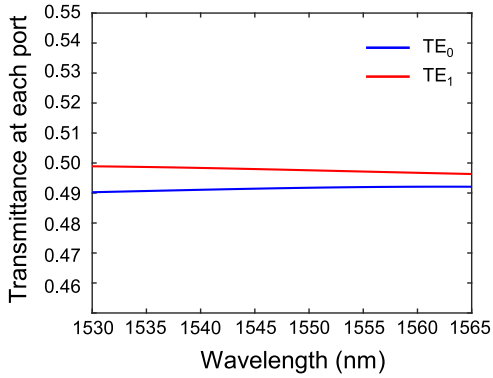

Fig. 10. Simulated wavelength dependence of the transmittance to each output port for the optimally designed mode-independent Y-splitter.

TABLE I
Obtained $\mathbf{w}$ (μM) of the Y-splitter After Optimization

w_1	w_8	w_8	w_8	w_8	w_8	w_8	w_8	w_9	w_{10}	w_{11}	w_{12}	w_{13}
0.85	0.95	1.05	1.15	1.2	1.3	1.33	1.44	1.41	1.35	1.34	1.4	1.3

interpolation of these 13 discrete points. The parameters $\mathbf{w}$ are then optimized to achieve mode-independent splitting through the PSO algorithm [22], which is one of the genetic algorithms. The optimization procedure is given in Fig. 9. The parameters G and S are the numbers of generations and seeds in each generation, respectively. Here, we set $G = 30$ and $S = 20$. The wave propagation is calculated by the 3D-FDTD method. We define the cost function f_{n} as

$$f_n = |T_{\mathrm{port1,\ TE_0}} - T_{\mathrm{port2,\ TE_0}}| + |T_{\mathrm{port1,\ TE_1}} - T_{\mathrm{port2,\ TE_1}}| \tag{A1}$$

where $T_{\mathrm{port1,TE}i}$ and $\mathrm{T}_{\mathrm{port2,TE}i}$ $(i = 0, 1)$ denote the transmittance of Y-splitter to each output port for the TE_i modes. After calculating S cost functions, $\mathbf{w}$ is updated according to the PSO algorithm. This procedure is repeated G times to derive the final optimized geometry. The derived $\mathbf{w}$ after convergence is listed in Table I.

The simulated light propagation through the optimized structure is shown in Fig. 3(b). Fig. 10 shows the calculated wavelength dependence of the transmittance to each output port. We can confirm that nearly equal splitting is obtained for both TE_0 and TE_1 modes over the entire C band.

ACKNOWLEDGMENT

RT acknowledges Yuto Suzuki, Taichiro Fukui, and Toshikazu Umezaki for fruitful discussions.

REFERENCES

[1] D. Soma et al., "10.16 Peta-bit/s dense SDM/WDM transmission over 6-mode 19-core fibre across C+L band," *J. Lightw. Technol.*, vol. 36, no. 6, pp. 1362–1368, Mar. 2018.

[2] G. Rademacher et al., "10.66 Peta-bit/s transmission over a 38-core-three-mode fiber," in *Proc. Opt. Fiber Commun. Conf.*, San Diego, CA, USA, 2020, Paper Th3H.1.

[3] B. J. Puttnam, G. Rademacher, and R. S. Luís, "Space-division multiplexing for optical fiber communications," *Optica*, vol. 8, no. 9, pp. 1186–1203, Sep. 2021.

[4] R. Ryf et al., "Space-division multiplexing over 10 km of three-mode fiber using coherent 6×6 MIMO processing," in *Proc. Opt. Fiber Commun. Conf.*, Los Angeles, CA, USA, 2011, Paper PDP.B10.

[5] N. K. Fontaine et al., "30×30 MIMO transmission over 15 spatial modes," in *Proc. Opt. Fiber Commun. Conf.*, Los Angeles, CA, USA, 2015, Paper Th5C.1.

[6] N. K. Fontaine et al., "Packaged 45-mode multiplexers for a graded index fiber," in *Proc. Eur. Conf. Opt. Commun.*, Rome, Italy, 2018, pp. 1–3.

[7] R. Ryf et al., "High-spectral-efficiency mode-multiplexed transmission over graded-index multimode fiber," in *Proc. Eur. Conf. Opt. Commun.*, Rome, Italy, 2018, pp. 1–3.

[8] J. Wang, S. Chen, and J. Liu, "Orbital angular momentum communications based on standard multi-mode fiber (invited paper)," *APL Photon.*, vol. 6, no. 6, Jun. 2021, Art. no. 060804.

[9] N.-P. Diamantopoulos, B. Shariati, and I. Tomkos, "On the power consumption of MIMO processing and its impact on the performance of SDM networks," in *Proc. Opt. Fiber Commun. Conf.*, Los Angeles, CA, USA, 2017, Paper Th2A.18.

[10] C. R. Doerr, "Proposed architecture for MIMO optical demultiplexing using photonic integration," *IEEE Photon. Technol. Lett.*, vol. 23, no. 21, pp. 1573–1575, Nov. 2011.

[11] A. Annoni et al., "Unscrambling light - automatically undoing strong mixing between modes," *Light: Sci. Appl.*, vol. 6, no. 12, Dec. 2017, Art. no. e17110.

[12] N. K. Fontaine et al., "Space-division multiplexing and all-optical MIMO demultiplexing using a photonic integrated circuit," in *Proc. Opt. Fiber Commun. Conf.*, Los Angeles, CA, USA, 2012, Paper PDP5B.1.

[13] R. Tanomura, R. Tang, G. Soma, S. Ishimura, T. Tanemura, and Y. Nakano, "All-optical dual-polarization MIMO processor based on integrated optical unitary converter," in *Proc. Eur. Conf. Opt. Commun.*, Basel, Switzerland, 2022, pp. 1–4.

[14] J.-F. Morizur et al., "Programmable unitary spatial mode manipulation," *J. Opt. Soc. Amer. A*, vol. 27, no. 11, pp. 2524–2531, Nov. 2010.

[15] G. Labroille, B. Denolle, P. Jian, P. Genevaux, N. Treps, and J.-F. Morizur, "Efficient and mode selective spatial mode multiplexer based on multi-plane light conversion," *Opt. Exp.*, vol. 22, no. 13, pp. 15599–15607, Jun. 2014.

[16] R. Tang, T. Tanemura, and Y. Nakano, "Integrated reconfigurable unitary optical mode converter using MMI couplers," *IEEE Photon. Technol. Lett.*, vol. 29, no. 12, pp. 971–974, Jun. 2017.

[17] M. Y. Saygin, I. V. Kondratyev, I. V. Dyakonov, S. A. Mironov, S. S. Straupe, and S. P. Kulik, "Robust architecture for programmable universal unitaries," *Phys. Rev. Lett.*, vol. 124, no. 1, Jan. 2020, Art. no. 010501.

[18] S. Ishimura, T. Fukui, R. Tanomura, G. Soma, Y. Nakano, and T. Tanemura, "64-QAM self-coherent transmission using symmetric silicon photonic stokes vector receiver," in *Proc. Opt. Fiber Commun. Conf.*, San Diego, CA, USA, Mar. 2022, Paper M4J.6.

[19] D. Dai and J. E. Bowers, "Novel concept for ultracompact polarization splitter-rotator based on silicon nanowires," *Opt. Exp.*, vol. 19, no. 11, pp. 10940–10949, May 2011.

[20] D. Dai, Y. Tang, and J. E. Bowers, "Mode conversion in tapered submicron silicon ridge optical waveguides," *Opt. Exp.*, vol. 20, no. 12, pp. 13425–13439, Jun. 2012.

[21] W. D. Sacher, T. Barwicz, B. J. F. Taylor, and J. K. S. Poon, "Polarization rotator-splitters in standard active silicon photonics platforms," *Opt. Exp.*, vol. 22, no. 4, pp. 3777–3786, Feb. 2014.

[22] Y. Zhang et al., "A compact and low loss Y-junction for submicron silicon waveguide," *Opt. Exp.*, vol. 21, no. 1, pp. 1310–1316, Jan. 2013.

[23] R. Tang, T. Tanemura, and Y. Nakano, "Robust reconfigurable optical mode mux/demux using multiport directional couplers," in *Proc. Opto-Electron. Commun. Conf. Photon. Glob. Conf.*, 2017, Singapore, doi: 10.1109/OECC.2017.8114996.

[24] R. Tanomura, R. Tang, S. Ghosh, T. Tanemura, and Y. Nakano, "Robust integrated optical unitary converter using multiport directional couplers," *J. Lightw. Technol.*, vol. 38, no. 1, pp. 60–66, Jan. 2020.

[25] R. Tang et al., "Reconfigurable all-optical on-chip MIMO three-mode demultiplexing based on multi-plane light conversion," *Opt. Lett.*, vol. 43, no. 8, pp. 1798–1801, Apr. 2018.

[26] R. Tanomura et al., "Monolithic InP optical unitary converter based on multi-plane light conversion," *Opt. Exp.*, vol. 28, no. 17, pp. 25392–25399, Aug. 2020.

[27] R. Tang, R. Tanomura, T. Tanemura, and Y. Nakano, "Ten-port unitary optical processor on a silicon photonic chip," *ACS Photon.*, vol. 8, no. 7, pp. 2074–2080, Jul. 2021.

[28] R. Tanomura, R. Tang, T. Tanemura, and Y. Nakano, "Integrated InP optical unitary converter with compact half-integer multimode interferometers," *Opt. Exp.*, vol. 29, no. 26, pp. 43414–43420, Dec. 2021.

[29] M. Bachmann, P. A. Besse, and H. Melchior, "General self-imaging properties in $N \times N$ multimode interference couplers including phase relations," *Appl. Opt.*, vol. 33, no. 18, pp. 3905–3911, Jun. 1994.

[30] M. Bachmann, P. A. Besse, and H. Melchior, "Overlapping-image multimode interference couplers with a reduced number of self-images for uniform and nonuniform power splitting," *Appl. Opt.*, vol. 34, no. 30, pp. 6898–6910, Oct. 1995.

[31] M. Ito, T. Fukui, T. Tanemura, and Y. Nakano, "Compact symmetric polarization rotator-splitter on InP," *Opt. Exp.*, vol. 30, no. 3, pp. 4179–4188, Jan. 2022.

[32] M. Ma, H. Shoman, K. Tang, S. Shekhar, N. A. F. Jaeger, and L. Chrostowski, "Automated control algorithms for silicon photonic polarization receiver," *Opt. Exp.*, vol. 28, no. 2, pp. 1885–1896, Jan. 2020.

[33] X. Wang, Y. Zeng, R. Liao, C. Zhao, H. Wu, and M. Tang, "Mach-Zehnder interferometer based endlessly adaptive polarization controller on silicon-photonic platform," in *Proc. Opt. Fiber Commun. Conf.*, San Diego, CA, USA, 2021, Paper Th1A.33.

[34] S. Ishimura, K. Nishimura, Y. Nakano, and T. Tanemura, "Polarization-diversity Stokes-analyzer-based coherent receiver," *Opt. Exp.*, vol. 27, no. 6, pp. 9071–9078, Mar. 2019.

[35] R. Tanomura, R. tang, T. Umezaki, G. Soma, T. Tanemura, and Y. Nakano, "Scalable and robust photonic integrated unitary converter based on multiplane light conversion," *Phys. Rev. Appl.*, vol. 27, no. 2, Feb. 2022, Art. no. 024071.